Journal of Advances in Nanomaterials, Vol. 2, No. 1, March 2017
https://dx.doi.org/10.22606/jan.2017.21002

Magnetic Fe_3O_4@G-C_3N_4 Nanocomposites for Visible Light Photocatalysis of RhB

Peitao Liu, Qiang Xu, Daqiang Gao*, Shoupeng Shi, Baorui Xia

Key Laboratory for Magnetism and Magnetic Materials of MOE, Lanzhou University, Lanzhou 730000, P. R. China.
Email: gaodq@lzu.edu.cn

Abstract. Visible light-responsive Fe_3O_4@g-C_3N_4 nanocomposites were prepared by hydrothermal method with g-C_3N_4 nanosheets as the substrates. The photocatalytic performances of the Fe_3O_4@g-C_3N_4 nanocomposites were evaluated in photo Fenton-like discoloration of RhB dye using H_2O_2 as an oxidant under visible-light irradiation. Meanwhile, the reusability and magnetic properties were also investigated. The results revealed that the Fe_3O_4@g-C_3N_4 nanocomposites showed considerable photocatalytic activity, and exhibited excellent reusability with almost no change after four runs, and more importantly, Fe_3O_4@g-C_3N_4 nanocomposites could be recovered magnetically. Therefore, the fabricated Fe_3O_4@g-C_3N_4 nanocomposite photocatalyst is a promising candidate for energy conversion and environmental remediation.

Keywords: Hydrothermal method, magnetic Fe_3O_4@g-C_3N_4 nanocomposites, photo Fenton-like, photocatalysis.

1 Introduction

Contamination of groundwater by persistent organic substances such as dyes or agrichemicals has been a worldwide environmental problem for decades. Effluents from the textile industries are important sources of water pollution, because dyes in wastewater undergoes chemical as well as biological changes, consume dissolved oxygen, destroy aquatic life and endanger human health. Therefore, it is necessary to treat textile effluents prior to their discharge into the receiving water[1-6].With the intensive development of materials research, various micro- and nano-materials have already been adopted for the treatment of environmental pollutants due to their excellent photocatalytic activities.

As an analogue of graphite, the graphitic carbon nitride (g-C_3N_4) possesses a stacked 2D structure and is the most stable allotrope of carbon nitride under ambient conditions[7]. More recently, graphitic carbon nitride was found to be a typical metal-free polymeric semiconductor material with a suitable band gap to absorb visible-light radiation and unique properties[8]. g-C_3N_4 is composed of carbon and nitrogen only, and the optical band gap was determined to be 2.7 eV. In addition, g-C_3N_4 semiconductor is stable under light irradiation in solution with pH=0-14 due to the strong covalent bands between carbon and nitride atoms[9]. These superior properties imply that the metal-free g-C_3N_4 has promising potential in photocatalysis fields. However, there are also many drawbacks for the g-C_3N_4 materials, which include low specific surface area, and high recombination rate of photogenerated electron-hole pairs. Therefore, many attempts have been made to improve the photocatalytic performance of g-C_3N_4, such as noble metal deposition[10], preparation of nano/porous g-C_3N_4[11,12], protonating g-C_3N_4 by strong mineral acids[13], and constructing a heterojunction composite with another semiconductor[14-19].

Ferriferrous oxide (Fe_3O_4) as a magnetic material has attracted more attention in various fields including ultrahigh-density magnetic recording, magnetic fluid, and biomedical materials[20,21]. Interestingly, Fe_3O_4 can be considered as a conductor because its conductivity is as high as 1.9×10^6 S m^{-1}, which is different from the other semiconductor characteristic of most metal oxide materials[22]. Meanwhile, Fe_3O_4 has matching conduction and valence bands with g-C_3N_4. The coupling of Fe_3O_4 with g-C_3N_4 can promote both the light response and the electron-hole pair separation; the higher photocatalytic activity it thus expected. Rhodamine B (RhB) was used as a model compound to investigate the activities of ferriferrous oxide and graphitic carbon nitride nanocomposites (Fe_3O_4@g-C_3N_4 nanocomposites) under sunlight. The reaction kinetics, dye degradation mechanism, and material stability, as well as the roles of g-C_3N_4 and Fe_3O_4 were

comprehensively studied. This research provides a novel practical approach for the use of heterogeneous photo-Fenton-like system (Fe_3O_4@g-C_3N_4 nanocomposites /H_2O_2/vis) in the efficient treatment of dye effluent. In addition, our findings suggest that the as-prepared hybrids can act as an efficient catalyst with some advantageous properties, such as easy magnetical separation, excellent recyclability and wide application, which may hold great potential for the actual application in treatment of water pollution.

2 Experimental

2.1 Synthesis and Preparation

All of the starting reagents used in this research are of analytical purity and used without further purification. g-C_3N_4 nanosheet was prepared by directly heating melamine at 500 °C in a furnance for 2 h.

In a typical synthesis process of Fe_3O_4 particals, 1 g $FeSO_4{\cdot}7H_2O$ was dissolved into 4 ml of hydrazine hydrate under magnetic stirring. Then the solution was transferred to a Teflon-lined stainless steel autoclave and maintained at 150 °C for 20 h before being cooled down in air.

In the process of preparing Fe_3O_4 particals, different amounts of g-C_3N_4 (1 g, 1.5 g, 2 g, 2.5 g respective) were added into a Teflon-lined stainless steel autoclave as substrates. The obtained Fe_3O_4@g-C_3N_4 nanocomposites with different contents of g-C_3N_4 were named as Fe_3O_4@g-C_3N_4 (S1), Fe_3O_4@g-C_3N_4 (S1.5), Fe_3O_4@g-C_3N_4 (S2), Fe_3O_4@g-C_3N_4 (S2.5). The schematic representation for the synthesis of g-C_3N_4@Fe_3O_4 nanocomposites is illustrated in Figure 1.

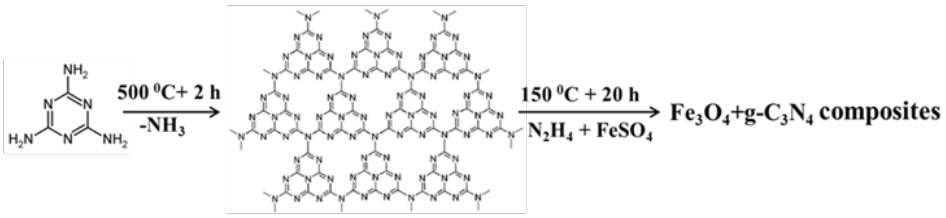

Figure 1. Illustration of the synthesis process of Fe_3O_4@g-C_3N_4 nanocomposites.

2.2 Characterizations

X-ray diffractometry (XRD) for the crystal structure of the products was carried out in a Philips/ X' Pert PRO diffractometer with Cu $K\alpha$ radiation. Thermogravimetric analysis (TGA) was carried out from room temperature to 1000 °C under nitrogen atmosphere. The magnetization curves were measured at room temperature under a varying magnetic field from -10000 to 10000 Oe on a MicroSense EV9 vibrating sample magnetometer (VSM). Spectra of Fourier transform infrared spectroscopy (FTIR) spectra of samples were recorded using a Niclet Nexus 670 spectrometer at room temperature. The morphology and structure of the Fe_3O_4@g-C_3N_4 nanocomposites were characterized by a transmission electron microscope (TEM) (FEI Tecnai TM G2 F30). The chemical nature of C, N, Fe, O have been studied using X-ray photoelectron spectroscopy (XPS) in VG Scientific ESCALAB-210 with Mg $K\alpha$ X-ray. The binding energy was referenced to C 1 s line at 284.6 eV for calibration.

2.3 Photocatalytic Activity

The photocatalytic activity of the samples was evaluated by the degradation of RhB and MO dye under visible light irradiation. An aqueous solution of RhB (MO) (50 ml, 20 mg l^{-1}) was placed in a glass, and a 50 mg photocatalyst was added under stirring. Then 1 ml H_2O_2 was added in it. Photocalytic activity of the sample was evaluated under sunlight. At certain time intervals, a certain amount of the solution was taken out and a magnet was used to remove the photocatalyst particles. Then the filtrates were analyzed by recording variations of the absorption band maximum (553 nm, 464 nm) in the UV-vis spectra of RhB by using a UV-vis spectrophotometer. In addition, the recyclability of Fe_3O_4@g-C_3N_4 nanocomposites were investigated. After each catalytic run, the solid sample was collected to perform subsequent photoreaction cycles.

3 Results and Discussion

3.1 Characterization

To calculate the content of Fe_3O_4 nanoparticles on g-C_3N_4 sheets, TGA was performed on Fe_3O_4@g-C_3N_4 nanocomposites under N_2 atmosphere from room temperature to 1000 °C. As can be seen from Figure 2, the decomposition of g-C_3N_4 starts at 300 °C and is completed about 750 °C, which is attributed to the burning of g-C_3N_4[23]. The residual weight fractions of the different nanocomposites (S1, S1.5, S2, and S2.5) were found to be 11.1, 9.5, 7.8, and 6.7%, which are considered to be the contents of Fe_3O_4 in the Fe_3O_4@g-C_3N_4 nanocomposites.

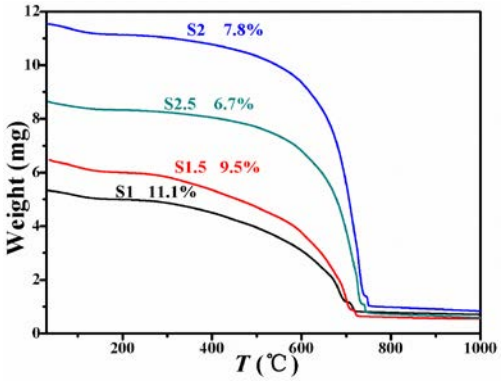

Figure 2. TGA curves of S1, S1.5, S2, and S2.5 photocatalysts.

The XRD patterns of the pure g-C_3N_4, pure Fe_3O_4, Used (S2.5 was used by photocatalyst) and Fe_3O_4@g-C_3N_4 nanocomposites are shown in Figure 3a. In the case of g-C_3N_4, the strong peak located at 27.21° was the typical interplanar stacking peak of conjugated aromatic systems. The other peak at 12.81° belongs to an in-planner structural packing motif. Both peaks were the characteristic peaks commonly found in carbon nitride[24]. The XRD patterns of pure Fe_3O_4, the observed diffraction peaks are in good agreement with those reported in the literature for pure face-centered-cabic Fe_3O_4[25,26]. For Fe_3O_4@g-C_3N_4 nanocomposites, the feature peaks of both g-C_3N_4 and Fe_3O_4 are detectable, indicating that Fe_3O_4 has been successfully loaded on g-C_3N_4. Moreover, for the used sample, the characteristic peaks were similar to primitive Fe_3O_4@g-C_3N_4 nanocomposites.

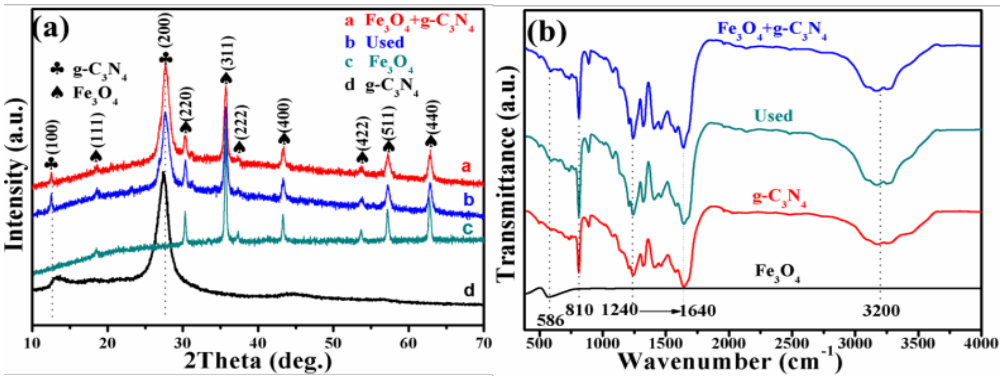

Figure 3. (a) XRD patterns, (b) FI-IR specture of g-C_3N_4, Fe_3O_4, Used, and Fe_3O_4@g-C_3N_4 nanocomposites.

FT-IR spectra of Fe_3O_4, g-C_3N_4, Used and Fe_3O_4@g-C_3N_4 nanocomposites were presented in Figure 3b. For the pure Fe_3O_4, the peak at 586 cm^{-1} is assigned as the symmetric stretching vibration of the Fe-O band in the tetrahedral FeO_6 groups of spinel-type compounds[27]. In the case of pure g-C_3N_4, characteristic bands in the region ranging from 1240 to 1640 cm^{-1} are attributed to either trigonal C-N (-C)-C (full condensation) or bridging C-NH-C units[28]. The sharp peak at 810 cm^{-1} was ascribed to the breathing

vibration of the triazine units. Furthermore, all the characteristic peaks of g-C_3N_4 and Fe_3O_4 were observed in the Fe_3O_4@g-C_3N_4 nanocomposites. Obviously the characteristic peaks of the Used sample were similar to Fe_3O_4@g-C_3N_4 nanocomposites.

Figure 4 shows TEM and high-resolution TEM (HRTEM) images of Fe_3O_4@g-C_3N_4 nanocomposites (sample S2.5). The TEM image (Figure 4a) reveals that Fe_3O_4 nanoparticles were successfully deposited on the surface of the g-C_3N_4 sheet by the in situ growth mechanism: almost no free Fe_3O_4 nanoparticles were found outside of the g-C_3N_4 sheet, which also prevented the agglomeration of Fe_3O_4 nanoparticles. The size of the Fe_3O_4 nanoparticles was found to be around 60nm to 100nm. The HRTEM image (Figure 4b) confirms the heterostructure in the Fe_3O_4@g-C_3N_4 nanocomposite system, where the g-C_3N_4 sheet could serve as a support and surfactant to bind with Fe_3O_4 nanoparticles in the resulting composite system[29].

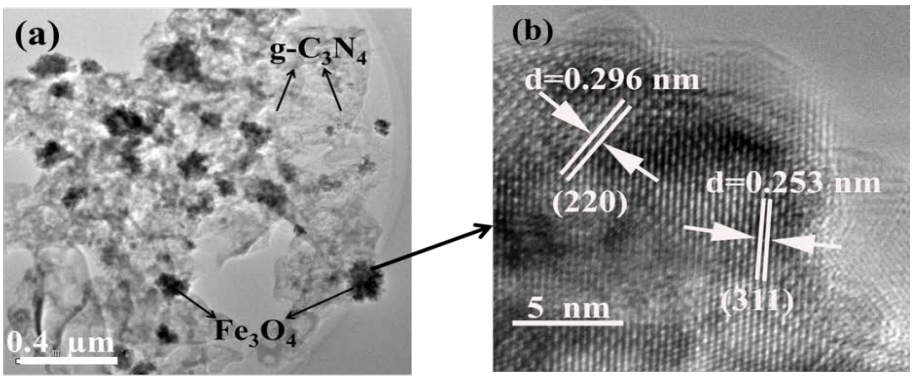

Figure 4. (a) TEM and (b) HRTEM image of Fe_3O_4@g-C_3N_4 (sample S2.5).

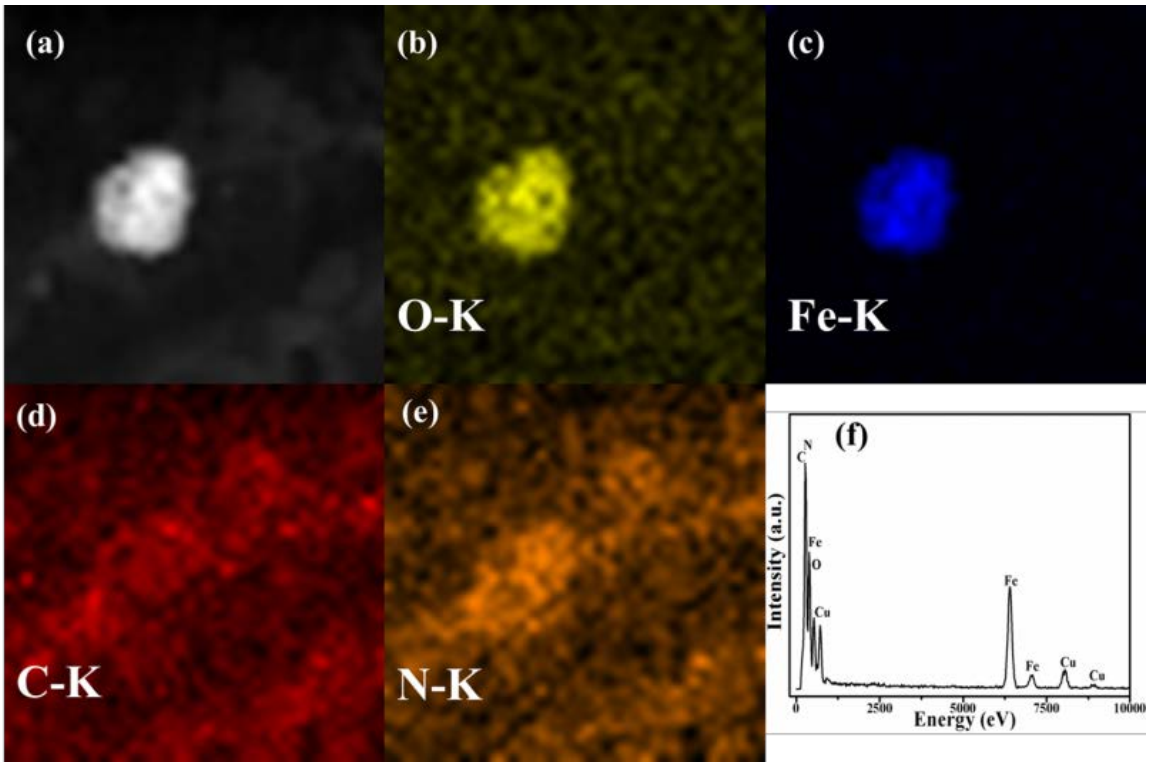

Figure 5. (a) HAADF-STEM image of S2.5. (b)-(e) O, Fe, C, and N element respectively. (f) EDS image of S2.5.

In order to determine the distribution of elements in the sample, the Fe_3O_4 nanoparticles and substrate were investigated by energy dispersive spectroscopic (EDS) analysis. Figure 5a shows the HAADF-STEM (High-angle annular dark-field scanning transmission electron microscopy) image of S2.5. In addition, Fe, C,

N, and O four elements are corresponding 5a to 5e respectively. Meanwhile, O and Fe elements exist only in Fe_3O_4 particles, but C and N elements exist only in substrate. The EDS analysis (Figure 5f) of the Fe_3O_4@g-C_3N_4 nanocomposite reveals the existence of C, N, Fe, O, and Cu (Cu from substrate) elements.

3.2 Photocatalytic Activity

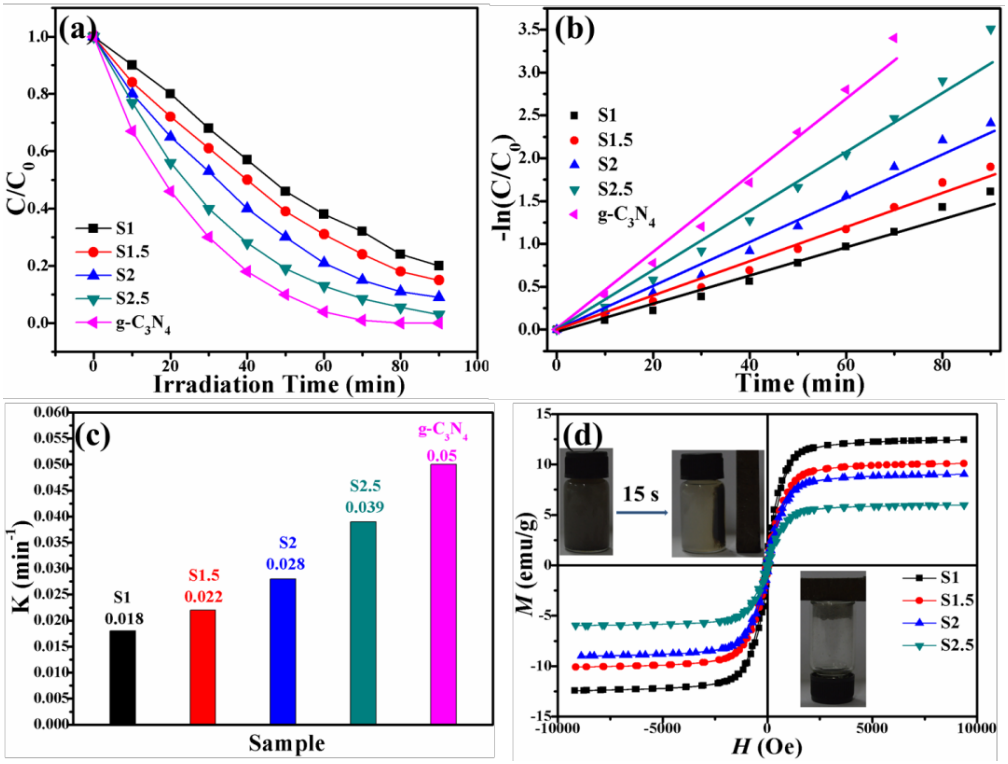

Figure 6. Photocatalytic properties of the obtained samples. (a) Photocatalytic degradation of RhB. (b) Plots of In(C/C_0) vs time. (c) The phodegradation rate of sample fitting. (d) M-H curve of samples at room temperature.

In this work, the photocatalytic performances of the samples were evaluated by the degrade of RhB aqueous solution at room temperature under visible-light irradiation (Figure 6). The initial concentration of the RhB suspension was measured and used as the initial concentration C_0. The Y axis is reported as C/C_0, where C is the actual concentration of RhB at the indicated reation time. The case of figure 6a shows the effects of concentration of Fe_3O_4 on the photocatalytic performance. As can be clearly seen in 6a, the decrease in the concentration of RhB is faster with S2.5 than other Fe_3O_4@g-C_3N_4 nanocomposites under the same experimental conditions. Though pure g-C_3N_4 is faster than S2.5 in degradation of RhB, but it is difficult to recycle. Sample S2.5 is because of its magnetic properties which make it easy to recycle and make the photocatalytic efficiency close to pure g-C_3N_4 (as can be seen in figure 6d). As shown in Figure 6b, the plots of In($C/C0$) versus irradiation time were linear, which indicates that the photodegradation of the RhB went through a pseudo-first –order kinetic reaction[30]. The optimum photocatalytic activity of Fe_3O_4@g-C_3N_4 nanocomposites at an Fe_3O_4 mass content of 6.7% under visible–light irradiation is higher than other compositions. In addition to the formula kt=-ln(C/C_0) fitting the RhB degradation rate, as shown in Figure 6c, it can be seen in four magnetic samples of magnetic separation recycling, S2.5 has the best catalytic effect of the samples. The magnetic properties of Fe_3O_4@g-C_3N_4 nanocomposites were also studied. As shown in Figure 6d, it is obvious that saturation magnetizations of these composites increased with an increase in Fe_3O_4 contents in the composites, suggesting that magnetic property of the composite could be rationally controlled by adjusting mass ratio of $FeSO_4$ to hydrazine hydrate in the present work. The magnetic separability of the composites was also examined by placing a magnet near the vessel. The upper left of Figure 6d shows that complete magnetic separation of S2.5 was achieved in 15 s by placing a magnet near the vessel. Then, the vessel was shaken

several seconds after the magnet was removed, and S2.5 was redispersed in the aqueous solution (bottom right corner of Figure 6d). These photographs further demonstrate that easy, fast separation and redispersion of S2.5 can be realized. Thus, the as-prepared catalysts can be concluded as stable and be recycled easily from solution.

3.3 Photocatalytic Activity

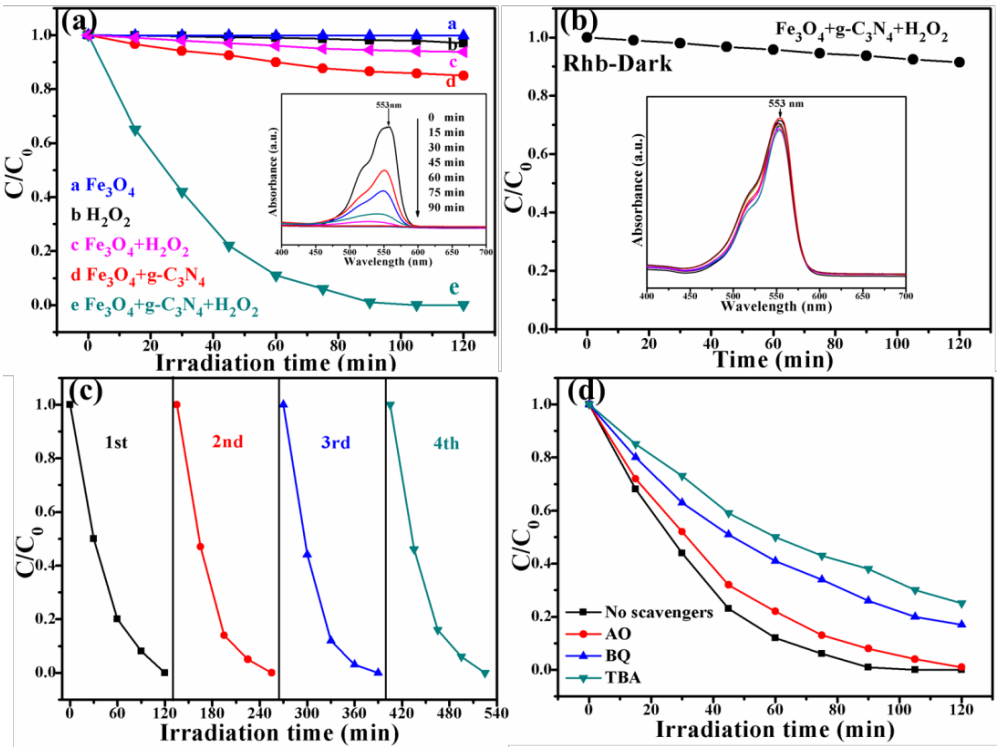

Figure 7. (a) Comparison of the photocatalytic performance of samples under different conditions. (b) Degradation of RhB by S2.5 in a dark condition. (c) Recyclability of S2.5 photocatalyst for the degradation of RhB under Visible-light irradiation. (d) Effects of different scavengers on the degradation of RhB by S2.5 and H_2O_2.

In order to study the photocatalytic properties of the g-C_3N_4@Fe_3O_4 nanocomposites, we selected S2.5 as a representative sample for discussion. The photocatalytic performances of the samples were evaluated by removal of RhB under visible-light irradiation (Figure 7a). As shown in Figure 7a, with $Fe3O_4$ sample in the absence of H_2O_2 or not, the discoloration hardly occurred under visible light illumination. Although the presence of H_2O_2 could increase the degradation of RhB, it is low. With the Fe_3O_4@g-C_3N_4 nanocomposite and visible light irradiation in the absence of H_2O_2 or not, the discoloration of RhB is obviously different, which suggests that Fe_3O_4@g-C_3N_4 and H_2O_2 are key in the degradation of RhB under visible-light irradiation. As shown in Figure 7b, the degradation efficiency of RhB reaches only 10% in a dark condition. It reveals light is an important role in degradation of RhB. In addition, the stability of photocatalysts was a crucial factor for their assessment and practical applications. Photocatalyst sample S2.5 with the highest performance was tested by four times' recycling reaction towards degradation of RhB. After every 2h of visible light irradiation, the sample was separated. As displayed in Figure 7c, the photocatalytic performance of S2.5 did not decrease obviously after four consecutive experiments. Therefore, the sample S2.5 photocatalyst showed high stability during the photocatalytic reaction[31]. In radical trapping experiments (Figure 7d), the degradation efficiency of RhB from 100% to 97% in the presence of ammonium oxalate (AO) compared to that with no radical scavengers, which indicated the photogenerated holes are not main sources for degradation of RhB, nor the sources of ·OH radicals. In general, the more positive the valence band potential, the stronger the oxidation ability of photogenerated holes, which is favored for better photocatalytic activity[32-34]. So it can be concluded that direct oxidation by holes is

negligible because the potential of photogenerated holes is not so positive that it cannot effectively oxidize dyes directly. Meanwhile, the degradation efficiencies of RhB reach 70% and 80% in the presence of tertiary butyl alcohol (TBA) and Benzoquinone (BQ), respectively, which indicates that ·OH radicals play a more crucial part than $\cdot O_2^-$ due to transformation of the parts of $\cdot O_2^-$ into ·OH radicals.

To further examine the stability of the photocatalysts, S2.5 photocatalysts were investigated by XPS analysis before and after photocatalytic reactions. The survey XPS spectrums of S2.5 and Used have the same elements, which were originated from before and after photodecolorization reaction of S2.5 (Figure 8a). As illustrated in Figure 8b, the binding energies of $Fe2p_{3/2}$ and $Fe2p_{1/2}$ were centered at 710.8eV and 724.6eV, respectively, which is consistent with the XPS data for Fe_3O_4[35]. These results indicate the Fe_3O_4 kept unchanged in the photocatalytic process.

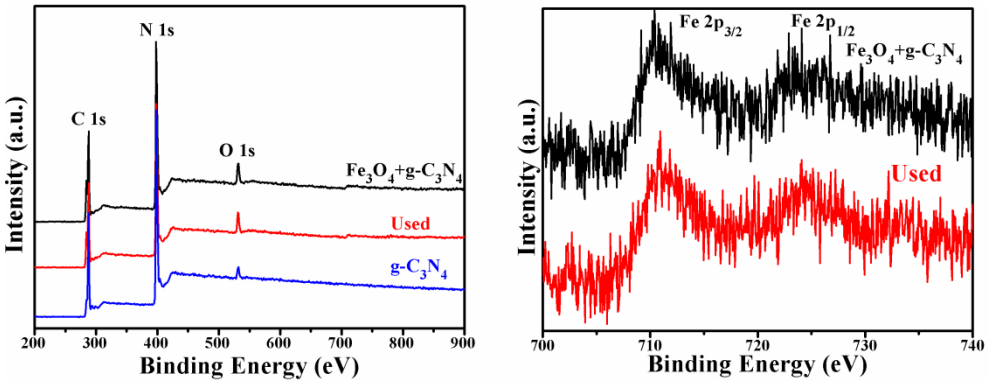

Figure 8. (a) Whole XPS spectrum of these samples. (b) XPS spectrum of Fe 2p before and after photocatalytic.

In order to evaluate ability of the Fe_3O_4@g-C_3N_4 nanocomposite (S2.5) for degradation of other dye pollutants, photocatalytic degradation of MO over the nanocomposite under the visible-light irradiation was considered. Figure 9 shows a plot of the degradation rate over nanocomposite. Meanwhile under the light irradiation for 180 min, nearly 100% of MO molecules were degraded on the nanocomposite, which indicates that the nanocomposite can degrade different dyes and has a wide range of application.

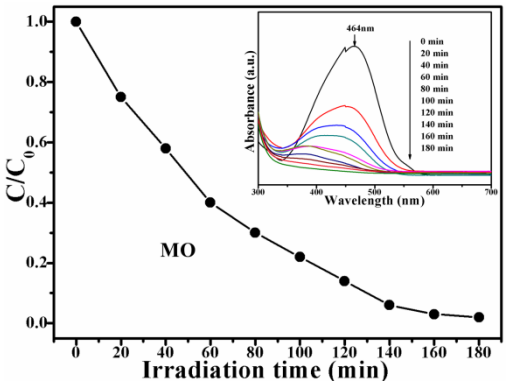

Figure 9. Photodegradation of MO on the Fe_3O_4@g-C_3N_4 nanocomposite.

Figure 10 illustrates the mechanism of charge separation and photoactivity of Fe_3O_4@g-C_3N_4 nanocomposites. Based on the band energy structure, both g-C_3N_4 and Fe_3O_4 are excited under visible light irradiation. The photoexcited holes and electrons are in their VB and CB, respectively. Under visible-light irradiation, the photoinduced electrons can easily be from the conduction band (CB) of g-C_3N_4 to the CB of use Fe_3O_4 because the CB level of Fe_3O_4 is lower than that of g-C_3N_4 (i.e., energy matching band structure is observed in the Fe_3O_4@g-C_3N_4 nanocomposites) [36,37]. Furthermore, because of the high conductivity of Fe_3O_4, the rate of electron transport is fast, which suppresses the direct recombination of photoinduced electron-hole pairs in the Fe_3O_4@g-C_3N_4 nanocomposites. Thus, Fe_3O_4 acts as an acceptor of

the photoinduced electrons from g-C_3N_4. Therefore, because of the presence of the Fe_3O_4@g-C_3N_4 interface, the chance of recombination of photoinduced electron-hole pairs is further successfully suppressed, leaving more charge carriers to form reactive species. The electrons in the CB of Fe_3O_4 are good reductants that could efficiently reduce the O_2 absorbed onto the composite catalyst surface into various reactive species ($O_2^{\cdot-}$, $HO_2^{\cdot}$, H_2O_2), subsequently leading to the formation of $^{\cdot}OH$ and oxidation of RhB into CO_2, H_2O, etc. The radical production could be expressed by reactions as follows:

$H_2O_2 \rightarrow O_2 + H_2O$

g-C_3N_4@Fe_3O_4 + hv $\rightarrow$ g-C_3N_4(h^+/e^-)@Fe_3O_4 (h^+/e^-)

$O_2 + e^- \rightarrow {}^{\cdot}O_2^-$

$H_2O_2 + e^- \rightarrow {}^{\cdot}OH + OH^-$

$H_2O_2 + O_2^- \rightarrow {}^{\cdot}OH + OH^- + O_2$

$Fe^{2+} + H_2O_2 \rightarrow Fe^{3+} + {}^{\cdot}OH + OH^-$

$Fe^{3+} + H_2O_2 \rightarrow Fe^{2+} + {}^{\cdot}OH + H^+$

$^{\cdot}OH$, O_2^-, h^+ + RhB $\rightarrow$ CO_2 + H_2O

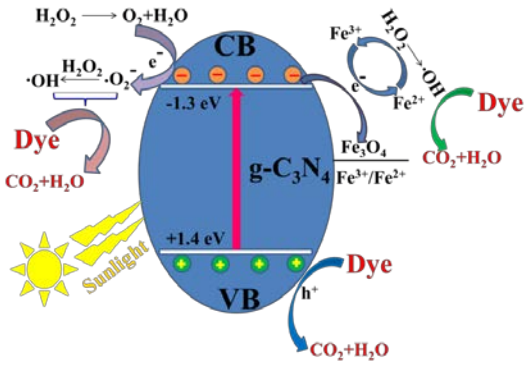

Figure 10. The mechanism of charge separation and photoactivity of g-C_3N_4@Fe_3O_4 nanocompositions under visible light irradiation.

4 Conclusions

In summary, we have successfully prepared Fe_3O_4@g-C_3N_4 nanocomposites via a facile hydrothermal method, characterized by XRD, FI-IR, TEM, HRTEM and UV-vis techniques and used for the photodegradation of RhB in aqueous solutions. The as-prepared Fe_3O_4@g-C_3N_4 nanocomposites have excellent activities and magnetic property for easy separation as well as durability on the elimination of the organic pollutants under visible light irradiation, maintaining high activities after four repeated uses. The optimal composite with 6.7wt% Fe_3O_4 showed a highest of photocatalytic efficiency. This work not only introduces a simple strategy to in-situ grow metal oxide nanoparticles on carbon nitride surfaces, but also demonstrates that the g-C_3N_4-based nanomaterials can serve as highly efficient photocatalysts for enviromental applications.

Supporting information. Experimental details, synthesis and characterization of g-C_3N_4 and Fe_3O_4 composites. XRD patterns, FI-IR spectrum, M-H curves, and XPS spectrum of g-C_3N_4@Fe_3O_4 nanocompositions. UV-vis spectroscopic changes for RhB and MO degradation, and the stability test for Fe_3O_4@g-C_3N_4 nanocomposites.

Acknowledgment. This work is supported by National Basic Research Program of China (Grant No. 2012CB933101), the National Natural Science Fundation of China (Grant No. 51371093, 51202101, 11474137 and 11034004), Program for Changjiang Scholars and Innovative Research Team in University (Grant No. IRT1251).

References

1. O. Ligrini, E. Oliveros, A. Braun, Chem. Rev., 1993, 93, 671.

2. M.F. Zhao, Z.B. Tang, P. Liu, J. Hazard Mater Chem., 2008, 158, 43.
3. A. Kaur, U. Gupta, J. Mater. Chem., 2009, 19, 8279.
4. M.F. Zhao, P. Liu, Micropor. Mesopor. Mater., 2008, 211, 419.
5. D.J. Yang, Z.F. Zheng, H.Y. Zhu, H.W. Liu, X.P. Gao, Adv. Mater., 2008, 20, 2777.
6. K.V. Baiju, S. Shukla, S. Biju, M.L.P. Reddy, K.G.K. Warrier, Mater. Lett., 2009, 63, 923.
7. M. Groenewolt and M. Antonietti, Adv. Mater., 2005, 17, 1789.
8. Wang, X, Maeda, K, Thomas, A, Takanabe, K, Xin, G, Carlsson, J. M, Domen, K, Antonietti, M. Nat. Mater., 2009, 8, 76.
9. A. Thomas, A. Fischer and F. Goettmann, et al. J. Mater. Chem., 2008, 18, 4893.
10. Liu, G, Niu, P, Sun, C. H, Smith, S. C, Chen, Z. G, Lu, G. Q, Cheng, H. M, J. Am. Chem. Soc., 2010, 132, 11642.
11. Goettmann , F, Fische r, A, Antonietti, M, Thomas, A. Angew. Chem., Int. Ed., 2006, 45, 4467.
12. Kailasam, K, Epping, J. D, Thomas, A, Losse, S, Junge, H, Energy Environ. Sci., 2011, 4, 4668.
13. Zhang, Y. J, Thomas, A, Antonietti, M, Wang, X. C, J. Am. Chem. Soc., 2009, 131, 50.
14. Yan, S. C, Lv, S. B, Li, Z. S, Zou, Z. G, Dalton Trans., 2010, 39, 1488.
15. Ge, L., Han, C. C., Liu, J., Appl. Catal., B 2011, 108, 100.
16. Yang, N, Li, G. Q, Wang, W. L, Yang, X. L, Zhang, W. F, J. Phys. Chem. Solid, 2011, 72, 1319.
17. Liu, Y, Chen, G, Zhou, C, Hu, Y. D, Fu, D. G, Liu, J, Wang, Q, J. Hazard. Mater., 2011, 190, 75.
18. Zhang, Y. J, Mori, T, Niu, L, Ye, J. H, Energy Environ. Sci., 2011, 4, 4517.
19. Ang, T. P, Chan, Y. M, J Phys. Chem. C 2011, 115, 15965.
20. Boal, A. K, Nanoparticles-Building Blocks for Nanotechnology, Rotello, V, Kluwer Academic/Plenum Publishers: New York, 2004,55, 1.
21. Perez, M, O'Loughlin, T, Simerone, F. J, Weissleder, R, Josephson, L. J., Am. Chem. Soc., 2002, 124, 2856.
22. Xi, G, Yue, B, Cao, J, Ye, J, Chem.-Eur. J. 2011, 17, 5145.
23. Wang, X.; Maeda, K.; Thomas, A.; Takanabe, K.; Xin, G.; Carlsson, J. M.; Domen, K.; Antonietti, M. Nat. Mater. 2009, 8, 76.
24. Wang, X. C., Maeda, K., Chen, X. F., Takanabe, K., Domen, K., Chem. Soc., 2009, 131, 1680.
25. Li, X, Huang, X, Liu, D, Wang, X., Song, S, Zhou, L, Zhang, H, J.Phys. Chem., C 2011, 115, 21567.
26. Xu, P, Zeng, G. M, Huang, D. L, Feng, C. L, Shuang, H, Zhao, M. H, Lai, C, Zhen, W, Huang, C, Xie, G. X, Liu, Z. F, A Review. Sci.Total Environ., 2012, 424, 1.
27. Y. Ding, L. Zhu, N. Wang, H. Tang, Appl. Catal. B 2013, 129, 153.
28. P. Niu, L. Zhang, G. Liu, H.-M. Cheng, Adv. Funct. Mater., 2012, 22, 4763.
29. Santosh Kumar, Surendar T, Bharat Kumar, Arabinda Baruah, Vishnu Shanker , J. Phys. Chem, 2013, 10, 1021.
30. Chalasani, R.; Vasudevan, S. ACS Nano, 2013, 7, 4093.
31. J. P. Zou, J. Ma, J. M. Luo, J. Yu, J. K. He, Y. T. Meng, Z. Luo, S. K. Bao, H. L. Liu, S. L. Luo, X. B. Luo, T. C. Chen and S. L. Suib, *Appl. Catal.,* 2015, 179, 220.
32. Li, X. H., Wang, X. C., Antonietti, M., Chem. Sci., 2012, 3, 2170.
33. Dong, H. J, Chen, G, Sun, J. X, Li, C. M, Yu, Y. G, Chen, D.H. Appl. Catal., 2013, 134, 46.
34. Yan, T. J, Long, J. L, Shi, X. C, Wang, D. H, Li, Z. H, Wang, X. X, Environ. Sci. Technol. 2010, 44, 1380.
35. T. Fujii, G.A. Sawatzky, F.C. Voogt, T. Hibma, K. Okada, Phys. Rev. B: Condens. Matter Mater. Phys. 1999 59 3195
36. Wang, X, Maeda, K, Thomas, A, Takanabe, K, Xin, G, Carlsson, J. M, Domen, K, Antonietti, M. Nat. Mater., 2009, 8, 76.
37. Xi, G, Yue, B, Cao, J, Ye, J, Chem.-Eur. J. 2011, 17, 5145.

